Journal of The Electrochemical Society, **154** (11) A1035-A1047 (2007)
0013-4651/2007/154(11)/A1035/13/$20.00 © The Electrochemical Society

Mesoscale Modeling of a Li-Ion Polymer Cell

Chia-Wei Wang[a,*] **and Ann Marie Sastry**[a,b,c,*,z]

[a]*Department of Mechanical Engineering,* [b]*Department of Biomedical Engineering, and* [c]*Department of Material Science and Engineering, University of Michigan, Ann Arbor, Michigan 48109-2125, USA*

Finite element models of a three-dimensional, porous cathode were constructed and analyzed by the COMSOL multiphysics package (version 3.2). Four types of cathode active material particles, arranged in both regular and random arrays, were modeled. Experimental studies of Li/PEO-$LiClO_4$/$Li_{1+x}Mn_2O_4$ (where $0 < x < 1$) were used to validate simulation results. Two parameters, Li ion diffusivity into $Li_{1+x}Mn_2O_4$ particles, and contact resistance at the interface between cathode particles and the current collector, were obtained by curve-fitting discharge curves of simulation results of regular array models, with $Li_{1+x}Mn_2O_4$ particles (3.6 μm) with experimental results. Diffusivities of Li ions were found to be 4×10^{-13}, 6×10^{-13}, 1×10^{-12}, and 5×10^{-12} cm^2/s for $Li_{1+x}Mn_2O_4$ particles sintered at 800, 600, 500, and 450°C, respectively. Contact resistances were found to be 3.5 Ω cm^2 for $Li_{1+x}Mn_2O_4$ particles prepared at 600 and 800°C, and 10.5 Ω cm^2 for particles prepared at 450 and 500°C. Regular arrays were shown to increase achievable capacity from 5 to 50% of the theoretical capacity, compared with random arrays, at C/10 for samples sintered at 500°C. Smaller particle sizes of active material particles were also shown to be beneficial for high power density applications and for low diffusivity active materials.
 [DOI: 10.1149/1.2778285]

Manuscript submitted March 20, 2007; revised manuscript received July 12, 2007. Available electronically September 21, 2007.

Though numerous, detailed experimental[1-9] and numerical[10-16] studies have been conducted to establish the benefits of specific types and morphologies of conductive additives in Li battery anodes and cathodes, simulations of battery performance generally disregard the details of material architecture and type. However, prior work has established not only that loading schema for conductive additives are important,[17-21] but also that conductive mechanisms are critical in predicting the ultimate conductive and performance gains, particularly in additives for cathodes.[22-24] These mechanisms cannot be properly accounted for in cell performance with continuum, porous electrode models[25-29] or equivalent circuit models;[30-40] nor can they be assessed with sufficient efficiency for simulation of large domains, using atomistic[41,42] or molecular dynamics[43,44] simulations.

Implementations with the capability of simulations at the particle scale have the potential to improve battery design, since experimental studies have established linkages between morphology of constituent materials and battery performance. Studies of the structures of the host matrix,[45] particle shape[46] and particle size[45-48] have established their importance on cycling performance, irreversible, and reversible capacity. Selection of appropriate materials, even for identical electrochemistries, is presently done on a trial-and-error basis[17,21] on multiple performance metrics, including conductivity, capacity, and rate capability.

A lithium-polymer cell, comprised of Li/PEO_{12}-$LiClO_4$/$Li_{1+x}Mn_2O_4$/Ni (negative electrode/polymer electrolyte/positive electrode/current collector), where $0 < x < 1$, reported previously[49] was used as a case study in the present work. Composition and dimensions of the cell are shown in Fig. 1. This particular study[49] was selected for two reasons. First, the study reported critical data required for mesoscale numerical simulation, including ionic conductivity of the electrolyte, open-circuit potential of the cathode materials, and discharge curves in terms of cell voltage and capacity.[49] Second, the relatively simple geometry of the cell, with a solid electrolyte and no separator, reduced computational intensity significantly from that of two porous electrodes and a semipermeable membrane, as with a typical Li-ion cell.

The objectives of this study were threefold:

1. To implement a three-dimensional (3D) finite element scheme for simulation of electrochemical performance of a porous cathode, taking direct account of active material and conductive additive particle types and morphologies. Transport of the ions and electrons was modeled for the active material and electrolyte phases individually; boundary conditions were implemented to simulate the interaction at the interface between phases.
2. Validation of the computational algorithm. A prior study published on a Li-polymer cell was used as a case study. This cell was selected because of the reduction in mesh requirements, given the regular shape of the anode, and lack of a separator.
3. Prediction of discharge performance for various cathode architectures. In this study, microstructure with both regular and random microstructures of the cathode particles was built, and effects on the shape of the discharge curve, and total capacity, were investigated.

Discharge conditions were selected to provide reasonable lifetime. Discharging spinel $Li_xMn_2O_4$ in the 3 V regime is not ideal for powering electronic devices requiring long cycle life, because of Jahn-Teller distortion, which leads to electrode structural failure due to 16% increase in the *c*/*a* ratio of the unit cell parameter during the cycling.[50] The $Li_{1+x}Mn_2O_4$ modeled here has a two-phase reaction process,[51] corresponding to formation of cubic $LiMn_2O_4$ and tetragonal $Li_2Mn_2O_4$. As Li ions are inserted into $Li_{1+x}Mn_2O_4$, the concentration of Mn^{3+} ions increases, reducing the crystal symmetry from cubic (*c*/*a* = 1) to tetragonal (*c*/*a* = 1.16). This 16% increase in the ratio of *c*/*a* induces particle strains with electrochemical cycling of Li ions in and out of the Mn_2O_4,[50] and may lead to loss of structural integrity and electrical contact. This is one of several possible reasons that rapid capacity loss of Li/$Li_{1+x}Mn_2O_4$ ($0 < x < 1$) cells was observed in Ref. 49.

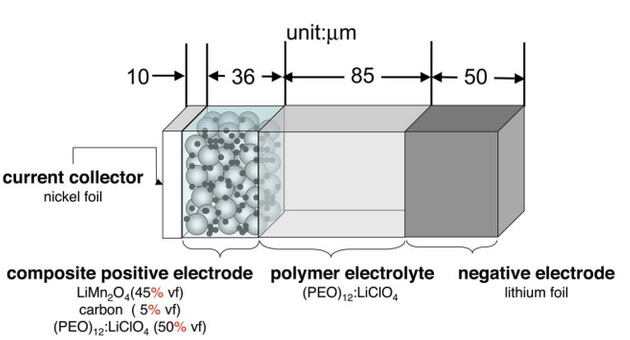

Figure 1. A schematic representation of the Li/PEO_{12}-$LiClO_4$/$Li_{1+x}Mn_2O_4$ configuration is shown. Dimensions and content of the electrode and polymer electrolyte are taken from Ref. 49.

* Electrochemical Society Active Member.
z E-mail: amsastry@umich.edu

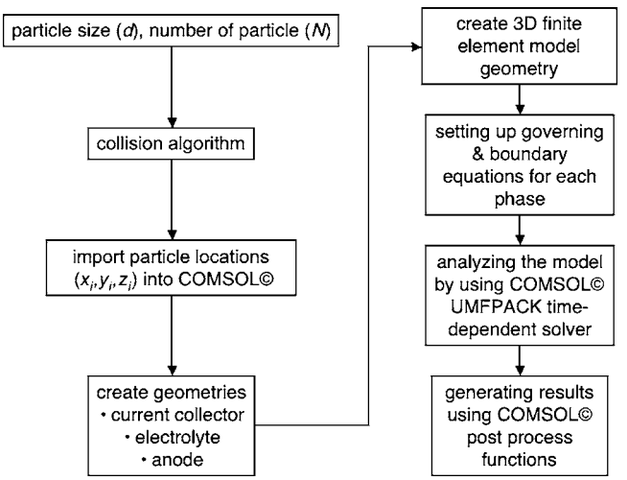

Figure 2. Simulation approach for the Li/PEO_{12}-$LiClO_4$/$Li_{1+x}Mn_2O_4$ system, via Comsol v.3.2.

Experimental

Materials assumptions.— The negative electrode was comprised of lithium metal, with a specific energy density of 3860 mAh/g; the positive electrode was comprised of $Li_{1+x}Mn_2O_4$ active material particles (95% vf), and ketjenblack carbon conductive additive particles (5% vf). $Li_{1+x}Mn_2O_4$ has a specific energy density of 151 mAh/g;[49] thus, the cell had an estimated capacity of 0.5 mAh/cm^2.[49] The current collector for the positive electrode was a nickel foil, rather than the now more commonly used copper foil. The polymer electrolyte was comprised of $LiClO_4$ with poly(ethylene oxide) (PEO), $-(CH_2-O-CH_2)_n-$, in a ratio of ([$-(CH_2-O-CH_2)-$]/[Li]) of 12. The pure polymer electrolyte phase was 86 μm thick, but also filled the porous, region of positive electrode with a volume fraction of 50%.

The effects of various sintering temperatures, 450, 500, 600, and 800°C, which were presumed to alter mobility of the Li ions in $Li_{1+x}Mn_2O_4$ active material particles, were studied in prior work.[49] The cell was experimentally discharged at a *C*/10 rate in Ref. 49.

Model development.— The process of implementation of a 3D finite element model using Comsol[52] is shown schematically as in Fig. 2, and first required model development, described in this section. Governing equations for the electrodes and polymer electrolyte involve Ohm's law, and basic transport laws, depending on the mobile species in each phase. In each case, the governing relations relate flux to mobile species concentration and electrical potential, while assuring that mass and charge conservation laws are obeyed. Ohm's law alone is sufficient to model regions in which electrons are the only mobile species. For multiple mobile species, the Nernst-Planck equation, relating flux to mobile species concentration and electrical potential, must be used, accounting for diffusion, migration and convection, with appropriate assumptions regarding concentrations, i.e., electrolyte theory. Conservation of mass must be used in conjunction with the Nernst-Planck equation, using a flux of specific mobile species balances explicitly. Relations used in each domain are described in the sections that follow.

Electrons are the only mobile species in the negative electrode, and in the current collector of the positive electrode. Thus, Ohm's law is used to determine the relationship between the current density and electrical potential in these regions.

In the polymer electrolyte and positive electrode, by contrast, both negatively and positively charged species must be mobile, to maintain electroneutrality and conserve mass. Thus, the total current is the summation of the motion of the two charged particles. The Nernst-Planck equation was thus used to model motion of charged species in these regions. Due to the high salt concentration in the polymer electrolyte, the coefficients of classical Nernst-Planck equation accounting for the diffusion, migration and convection were modified, using concentrated electrolyte theory. The underlying assumption for this modification was that the driving force for mobile species in concentrated solution is the gradient of the electrochemical potential.

Frequently, the electrochemical potential of an ionic species is expressed as a function of the electrostatic potential and concentration. In the 3D finite element model developed here, each phase was characterized by the concentrations of the ionic species and electrostatic potential, rather than in terms of electrochemical potential. Hence, the electrochemical potential was deduced from salt concentration and electrical potential.

In the positive electrode, the negative ions in $Li_{1+x}Mn_2O_4$ are relatively stationary; electroneutrality requires that electrons balance the transport of the Li ions into the positive electrode. The fluxes of negatively and positively charged species in the Nernst-Planck equation were thus obtained via use of Ohm's law and application of the diffusion equation, respectively. Finally, conservation of mass was enforced at the interface of the two phases. The interfaces between the negative electrode and current collector of the positive electrode were assumed to be electrically insulated, to conserve electrons in the domains of interest. Periodic boundary conditions were applied to corresponding interfaces between the electrolyte and positive electrode to conserve ionic species, ensuring that concentration and electrical potential were identical for opposite faces. The remaining interfaces among phases were assumed to conserve current density.

Details of governing equations and interfacial conditions are given in the labeled sections that follow. In all sections, index i was used to denote either the negative ($i = 1$) or positive ($i = 3$) electrode. Subscripts 1, 2, 3, and 4 were used to denote the phases within the cell, including lithium metal; polymer electrolyte; the particulate, composite $Li_{1+x}Mn_2O_4$; and the current collector of the positive electrode, respectively. Subscripts (1,2), (2,3), (2,4), and (3,4) were used to denote the interfaces between lithium metal and polymer electrolyte; polymer electrolyte and cathode particles; polymer electrolyte and cathode current collector; and cathode particles and current collector, respectively.

Electrode kinetics.— The charge-transfer reaction was assumed to occur at each interface between two phases, only. At the interface of lithium metal and polymer electrolyte, Li ions were dissociated from or deposited on lithium metal during the discharge-charge processes, as

$$\mathrm{Li} \underset{\text{charge}}{\overset{\text{discharge}}{\rightleftarrows}} \mathrm{Li^+} + \mathrm{e^-} \qquad [1]$$

Similarly, Li ions were exchanged with the available electrons on the surface of $LiMn_2O_4$. The electrochemical reaction at the interface between $LiMn_2O_4$ and the polymer electrolyte can be expressed as

$$\mathrm{Li^+} + \mathrm{LiMn_2O_4} + \mathrm{e^-} \rightleftarrows \mathrm{Li_2Mn_2O_4} \qquad [2]$$

The rate of reaction is related to the nature and previous treatment of the electrode surface, the composition of the electrolytic solution adjacent to the electrode, and the overpotential between the electrode and the electrolyte. The rate reactions of Eq. 1 and 2 can be modeled by the Butler-Volmer equation.[53-55] This relation is derived by the difference between the cathodic and anodic currents, which is a function of rate constants and concentrations. In this relation, it is assumed that the rate constants follow an Arrhenius relation, and the cathodic and anodic currents follow the Tafel equation[56] to relate overpotential to the charge current. Hence, the total rate of ion exchange, expressed as current density, $j_{i,2}$, is calculated as the difference between the rates of the anodic and cathodic reactions of Eq. 1 or 2, as

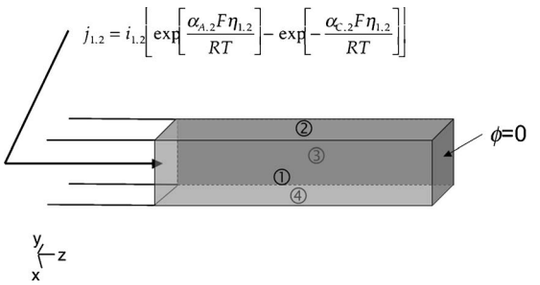

Figure 3. A schematic of the lithium metal foil with its boundary conditions: insulated boundary at the right plane, Butler-Volmer reaction boundary at the left plane, and four periodic boundaries as indicated by ①, ②, ③, and ④.

$$j_{i,2} = i_{i,2}\left[\exp\left[\frac{\alpha_{A,i}F\eta_{i,2}}{RT}\right] - \exp\left[-\frac{\alpha_{C,i}F\eta_{i,2}}{RT}\right]\right] \quad [3]$$

Anodic and cathodic transfer coefficients for the electrode $\alpha_{A,i}$,$\alpha_{C,i}$, respectively, are used to indicate the fractions of anodic and cathodic reactions induced by the overpotential, $\eta_{i,2}$.[57]

The surface overpotential, $\eta_{i,2}$, of Eq. 3 between two phases is the driving force for the charge-transfer reactions, and is defined as

$$\eta_{i,2} = \mathbf{\Phi}_i - \mathbf{\Phi}_2 - U_i \quad [4]$$

where $\mathbf{\Phi}_i$ and $\mathbf{\Phi}_2$ are the surface potential at the interface of electrode i and electrolyte phase, and U_i is the open circuit of electrode i. For the charge-transfer reaction of Eq. 1, U_i is set to zero, because the potential of the cell is measured relative to the lithium metal foil. U_i is set to the open-circuit potential of cathode particles, $Li_{1+x}Mn_2O_4$, for reaction of Eq. 2, provided previously.[49] The open-circuit potential, U_3, can be curve fitted with state of charge, x, by the fifth order of polynomial, as

$$U_3 = (-23.53x^5 + 52.43x^4 - 44.86x^3 + 18.4x^2 - 3.35x + 3.16) \quad [5]$$

As $\eta_{i,2}$ approaches zero, the driving force vanishes, and the reaction reaches equilibrium.

The exchange current density of Eq. 3, $i_{i,2}$, determines the rate of the reaction, and depends upon the reactant and product concentrations adjacent to the interface, following

$$i_{i,2} = K(c_i^{\max} - c_i)^{\alpha_{A,i}}(c_i)^{\alpha_{A,i}}(c_2^{\max} - c_2)^{\alpha_{C,i}}(c_2)^{\alpha_{C,i}} \quad [6]$$

where c_i,c_2 are Li ion concentrations at interface of electrode i and the polymer electrolyte. K is a rate constant, $c_i^{\max}$ is the maximum intercalation concentration of Li ions at the surface of electrode i, and $c_2^{\max}$ is the maximum concentration of Li ions permissible in the PEO. Hence, the exchange current density approaches zero as the Li ions reach either their maximum insertion concentration in the $LiMn_2O_4$ particle surface, or PEO at the interfaces of (1,2), and (2,3).

Mass transfer.— In the negative electrode (shown schematically in Fig. 3), electrons are the only mobile species. Electrons must be transferred from external circuitry to the interface, where Li ions are exchanged between the negative electrode and polymer electrolyte, following Eq. 1. The rate of electron transfer, $\mathbf{j}_1$, is driven by the electrical potential gradient in the negative electrode, Φ_1, and is expressed using Ohm's law, as

$$\mathbf{j}_1 = -\boldsymbol{\kappa}_1 \cdot \nabla \mathbf{\Phi}_1 \quad [7]$$

Electronic conductivity is written in tensorial form, $\boldsymbol{\kappa}_1$, to permit anisotropic material properties. Mass transfer in polymer electrolyte and positive active particles requires use of conservation of mass and charge, and concentrated solution theory for description of the motion for the charged species; the latter is required by the high salt concentration.

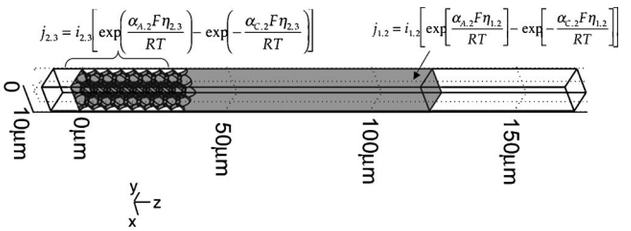

Figure 4. A schematic representation of the polymer electrolyte and two nonsymmetric boundaries.

The current in these two phases is expressed mathematically as the sum of the motions of charged species, as

$$I = F\sum_i z_i\mathbf{N}_i \quad [8]$$

where F is the Faraday's constant, z_i is the charged number of mobile species i, and $\mathbf{N}_i$ is the flux of the mobile species, i. Conservation of mass is expressed as

$$\frac{\partial c_i}{\partial t} = -\nabla \cdot \mathbf{N}_i + R_i \quad [9]$$

where c_i is the concentration of the mobile species i. R_i is the homogeneous chemical reaction in electrode surface, and is usually zero for the electrochemical system.[55] Electroneutrality is required for these two phases, following

$$\sum_i z_i c_i = 0 \quad [10]$$

The only difference in governing equations for these two phases is in the description of flux, $\mathbf{N}_i$, necessitated by the difference in the description of motions of charged species, explained as follows.

The polymer electrolyte, PEO_{12}-$LiClO_4$, is assumed to be binary, i.e., only positive and negative ionic species are assumed to be mobile. The movement of the Li ions during charge or discharge is thus balanced with negatively charged ions to satisfy electroneutrality. The polymer electrolyte phase includes the particle-free region between the negative and positive electrodes, and the volume excluded $Li_{1+z}Mn_2O_4$, depicted by the gray area of Fig. 4.

The driving forces for mass transfer in the polymer electrolyte are the fluxes of mobile species. Derivations of fluxes in the polymer electrolyte are based on the assumption that the solution is concentrated, because salt concentrations are generally high, i.e., greater than 1 M. Although the driving force for mass transfer in a concentrated solution is the gradient of the electrochemical potential only,[55] it is difficult to directly assess the electrochemical potential in a 3D finite element model. Fortunately, the gradient of the electrochemical potential can be decoupled into the gradients of salts concentration and electrical potential, as shown in Ref. 58; these variables are used in the 3D finite element model. Thus, the fluxes for the concentrated solution can be expressed in terms of gradients concentrations, c_i; the gradient of electrical potential, Φ_2; and activity coefficient, $f_\pm$. If the solvent velocity is negligible, the flux of the positive and negative ionic species can be expressed in terms of the gradients of the electrical potential, Φ_2, and salt concentrations, as

$$\mathbf{N}_+ = \left[-\nu_+\mathcal{D}_2\frac{c_T}{c_0} + \frac{2\kappa_2 t_-^0 t_+^0 RT}{c_+ z_+ F^2}\right]\left(1 + \frac{d\ln f_\pm}{d\ln c}\right)\nabla c_+ - \frac{\kappa_2 t_+^0}{z_+ F}\nabla\Phi_2$$

$$\mathbf{N}_- = \left[-\nu_-\mathcal{D}_2\frac{c_T}{c_0} + \frac{2\kappa_2 t_-^{02} RT}{c_- z_- F^2}\right]\left(1 + \frac{d\ln f_\pm}{d\ln c}\right)\nabla c_- - \frac{\kappa_2 t_-^0}{z_- F}\nabla\Phi_2 \quad [11]$$

where c_T and c_0 are total and solvent concentrations, $\mathcal{D}_2$ and κ_2 are the ionic diffusivity and conductivity of electrolyte, and ν_+ and ν_-

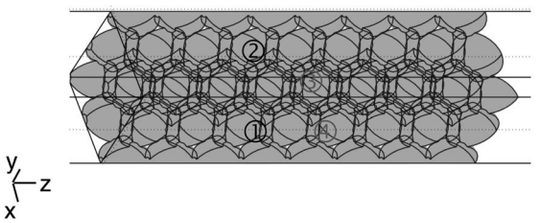

Figure 5. A schematic of the solid phase of $Li_{1+x}Mn_2O_4$.

are the numbers of cations and anions into which a molecule of electrolyte dissociates. A detailed derivation of Eq. 11 is included as the Appendix. Equation 11 has a form similar to the Nernst-Planck equation, with modified coefficients for the gradients of salts concentrations and electrical potential. Hence, the Nernst-Planck equations included in the "Chemical Engineering Module" of the Comsol multiphysics package (version 3.2) are used for modeling the fluxes of ionic species of polymer electrolyte, which also solves the mass balance of Eq. 9, simultaneously.

Li ions and electrons were assumed to be the main mobile species in the positive electrode of the heterogeneous, particulate $Li_{1+x}Mn_2O_4$ network (Fig. 5). The diffusion of the anions inside $Li_{1+x}Mn_2O_4$ is sufficiently slow such that mobile electrons must balance Li ion motion in the positive electrode, to maintain electroneutrality. Consequently, flux equations, including Eq. 11, in which the transference number t_+^0 is set to zero, were used to account the mass transfer of the positive electrode as

$$\mathbf{N}_+ = -D_3 \frac{c_T}{c_0}\left(1 + \frac{d \ln f_\pm}{d \ln c}\right) \nabla c_+$$

$$\mathbf{N}_- = \frac{\kappa_3}{F} \nabla \Phi_3 \qquad [12]$$

where $\mathbf{N}_+$ is the molar flux of Li ions in $Li_{1+x}Mn_2O_4$, and $\mathbf{N}_-$ is molar flux of electrons that is equivalent to the Ohm's law. D_3 and κ_3 are the ionic diffusivity and electrical conductivity of $Li_{1+x}Mn_2O_4$, respectively.

Electrons are the only mobile species in the nickel current collector. Thus, Ohm's law was employed to account for the rate of electron transfer in the nickel current collector, following

$$\mathbf{j}_4 = -\boldsymbol{\kappa}_4 \nabla \Phi_4 \qquad [13]$$

where κ_4 is the conductivity tensor of the current collector, and Φ_4 is the electrical potential of nickel current collector.

Interfacial conditions.— For the negative electrode, three interfacial conditions were used. First, the Butler-Volmer equation (Eq. 3) was used to model the exchange current density at the interface between the negative electrode and the polymer electrolyte. Second, the voltage at the top (in the z direction) of the Li metal foil (shown in Fig. 3) was set to zero, since the whole cell voltage was calculated relative to the negative electrode. Third, the values of inward currents were set to zero, since the remaining faces of the negative electrode were assumed to be electrical insulators, conserving electrons in the negative electrode.

For the polymer electrolyte, three interfacial conditions were employed. First, the Butler-Volmer equation (Eq. 3) was applied to model the exchange current densities at the interface between the negative electrode and the polymer electrolyte, and the interface between $Li_{1+x}Mn_2O_4$ particles and the polymer electrolyte (shown in Fig. 4). Second, the fluxes of two charged mobile species were set to zero at the interface of the electrolyte and cathode current collector, because ions do not diffuse to the nickel foil current collector of the positive electrode. Third, periodic boundary conditions are applied to four faces, which confine polymer electrolyte region as ①, ②, ③, and ④ indicated in Fig. 4.

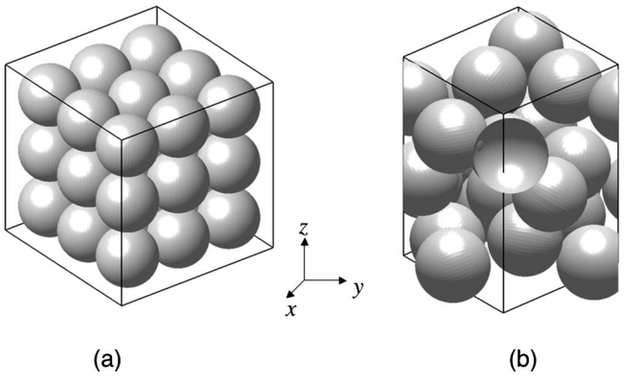

Figure 6. A schematic of particle arrangements in (a) a regular array, and (b) a random array.

For the positive electrode, three interfacial conditions were used. First, the Butler-Volmer equation (Eq. 3) was used to model the exchange current density of Li ions between the polymer electrolyte and $Li_{1+x}Mn_2O_4$. Second, the potential difference between the interface of positive active particles and nickel current collector due to imperfect bonding between them was modeled via contact resistance, R_C, as

$$\boldsymbol{\Phi}_3 - \boldsymbol{\Phi}_4 = j_{3,4} \cdot R_c \qquad [14]$$

This current density is governed by the rate of transfer of electrons. Thus, the rate of transfer of Li ions was set to zero at this interface, because Li ions were not exchanged in the current collector of positive electrode. Third, periodic boundary conditions were set for these interfaces, which confine the positive particulate network but are not adjacent to either current collector, or to the polymer electrolyte as indicated by ①, ②, ③, and ④ in Fig. 5.

For the current collector of the positive electrode, four different types of interfacial conditions were used. First, a potential drop at the interface of the positive active particles and current collector (Eq. 14) was used to model the imperfect bond between them. Second, the interfaces between the polymer electrolyte and the current collector were assumed to be electronically insulated, to assure no electron loss at these interfaces. Third, discharge current was set to exit at the bottom of the current collector. Fourth, periodic boundary conditions were applied to the remaining interfaces, which confine the positive current collector and are not adjacent to either the electrolyte or particles of the positive electrode.

Finite element implementation.— For finite element implementation, assumptions were required for particle sizes, arrangements, and material properties. Selections were made in order to span reasonable choices, based on prior work on similar cells, and both theoretical and experimental values for material properties.

Geometry and meshing.— Active material particle sizes and packing architectures were not given in Ref. 49. Similar cells[59-61] typically employ active material particles with diameters ranging from a few nm to 10 μm. In this study, active material particles of diameters, ϕ, of 3.6, 4.5, 6.0, and 12 μm were selected, for two main reasons. First, most particle sizes reported are smaller than 4 μm (e.g., Ref. 59-61). Second, prior work[62] has shown that smaller particle sizes offer better electrochemical performance, because of their larger surface areas.

These particles were assumed to be arranged in the positive electrode in both regular and random arrays, as shown in Fig. 6, to investigate the effect of such arrangements on performance. It has been observed in other contexts, including in geochemistry,[63] environmental modeling,[64] and other computation models,[65,66] that random architectures result in lower transport properties because of high tortuosity. Their volume fractions were about 52%, as in Ref. 49. The size of the representative volume ($W \times L \times H$) was set to

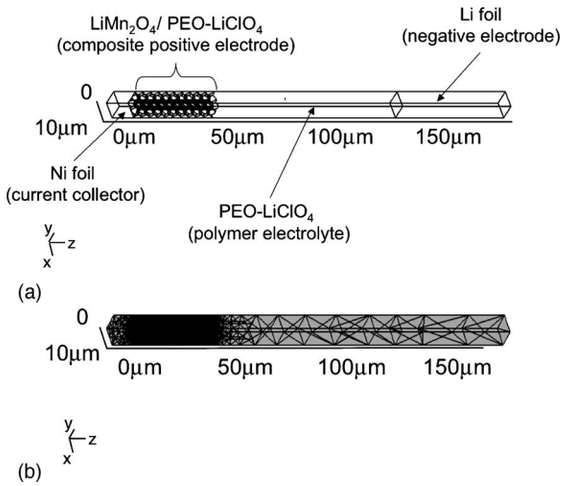

Figure 7. Finite element models, including (a) a 3D finite element model of Li/PEO-$LiClO_4$/$Li_{1+x}Mn_2O_4$ where the positive (cathode) electrode is a composite of a simple cubic lattice of $LiMn_2O_4$ particle and PEO-$LiClO_4$ polymer electrolyte with volume ratio (50:50); and (b) meshes of 3D finite element model.

approximately ($2\phi \times 2\phi \times t$), where t is the thickness of the composite cathode. Thus, there were four particles in a single layer for the simple cubic lattice model.

The number of layers in each model was calculated based on particle size. For example, there were three layers for the 12 μm network, but ten layers for the 3.6 μm network. Thus, a total of 12 particles were modeled in the simple cubic lattice structure model with particle sizes of 12 μm, but the total number of particles was increased to ~40 for 3.6 μm diameter arrangements. Construction of random arrays was accomplished using a dynamic collision algorithm with periodic boundary conditions.[16] This scheme prevented boundary effects, and allowed precise matching of volume fraction.

Finite element models of a whole cell were constructed and analyzed using the Comsol multiphysics package (version 3.2), following a four-step procedure. First, the domains of the positive current collector, particulate network of positive electrode, electrolyte, and negative electrode were built, as shown in Fig. 7a. Next, the whole cell model was meshed by using the Comsol mesh generator as shown in Fig. 7b using approximately 19,700–25,200 linear, tetrahedral elements for the various cases studied. Third, the governing equations, and interfacial conditions were set up, as described in the section on Finite element implementation. Finally, the Li ion concentration, electrical potential contours, cell voltage were obtained using postprocessing functions, after the whole cell model was solved.

The details of the particle packing architectures for both simple and random arrays were critical for model tractability. Random networks required more elements than the regular arrays because of the irregularity in the interstitial spaces among particles. Also, because conductive additive particles were not separately modeled, but rather the active particles of $Li_{1+x}Mn_2O_4$ were assumed to be conductive, they had to be percolated from the positive current collector (nickel foil) to the rest of the network to provide conductivity in the otherwise insulating medium. Thus, all particles in contact were assumed to be fused. This is a topic we have addressed elsewhere[67] for fibrous geometries, and will be the subject of future work as well. For the present study, though, a sufficient area of contact was selected to prevent meshing or convergence difficulty; the degree of interpenetration has been discussed elsewhere,[67] and may be applicable to the study of cathode particles in the future.

Material properties and model implementation.— Material properties were selected based upon $Li_{1+x}Mn_2O_4$,[21,49] PEO_{12}-$LiClO_4$ polymer electrolyte,[49,68-70] lithium metal,[71] and nickel foil current collector;[72] values are listed in Table I. The theoretical capacity of Li/PEO_{12}-$LiClO_4$/$Li_{1+x}Mn_2O_4$ cell was estimated to be about 0.5 mAh/cm^2 based on a value of 151 mAh/g for $Li_{1+x}Mn_2O_4$ and an energy density of ~440 Wh/kg, as discussed in Ref. 49. A $C/10$ rate, 0.05 mA/cm^2, was used as a constant discharge rate. The ionic diffusivity of polymer electrolyte, PEO-$LiClO_4$, was calculated based on the ionic conductivity of the electrolyte, following the modified Nernst-Einstein equation[73]

Table I. Values of parameters used in 3D finite element models. [Note that values marked with an asterisk (*) were estimated based on curve fitting].

Symbol	Name/description	Value	Unit	Reference
T	Working temperature	120	°C	49
c_0	Electrolyte concentration	2.07×10^{-3}	mol/cm^3	49
c_s	Initial lithium concentration in $Li_{1+y}Mn_2O_4$ as $y = 0$	1.13×10^{-2}	mol/cm^3	49
c_s^{max}	Maximum lithium concentration in $Li_{1+y}Mn_2O_4$ as $y = 1$	2.26×10^{-2}	mol/cm^3	49
κ_e	Ionic conductivity of electrolyte	3.80×10^{-3}	S/cm	68
D_e	Diffusivity of electrolyte	1.27×10^{-7}	cm^2/s	Eq. 15
t_+	Transference number	0.2		69
κ_s	Electronic conductivity of $Li_{1+y}Mn_2O_4$	5.56×10^{-2}	S/cm	21
D_s	Diffusivity of $Li_{1+y}Mn_2O_4$ heat-treated at 450°C	5.00×10^{-12}	cm^2/s	···
D_s	Diffusivity of $Li_{1+y}Mn_2O_4$ heat-treated at 500°C	1.00×10^{-12}	cm^2/s	···
D_s	Diffusivity of $Li_{1+y}Mn_2O_4$ heat-treated at 600°C	6.00×10^{-13}	cm^2/s	···
D_s	Diffusivity of $Li_{1+y}Mn_2O_4$ heat-treated at 800°C	4.00×10^{-13}	cm^2/s	···
R_c	Contact resistance between the cathode particles prepared at 600°C, 800°C, and nickel current collector	3.5	Ω cm^2	···
R_c	Contact resistance between the cathode particles prepared at 500°C, 450°C, and nickel current collector	10.5	Ω cm^2	···
κ_l	Electronic conductivity of lithium metal foil	1.08×10^5	S/cm	71
κ_4	Electronic conductivity of nickel metal foil	1.25×10^5	S/cm	72
α_a	Anodic apparent transfer coefficient	0.5		70
α_c	Cathodic apparent transfer coefficient	0.5		70
$i_{1,2}$	Exchange current density between lithium foil and electrolyte	8.50×10^{-1}	A/cm^2	
$i_{2,3}$	Exchange current density of between $Li_{1+y}Mn_2O_4$ and electrolyte	1.56×10^{-1}	A/cm^2	
I	Discharge current density ($C/10$)	0.05	mA/cm^2	49

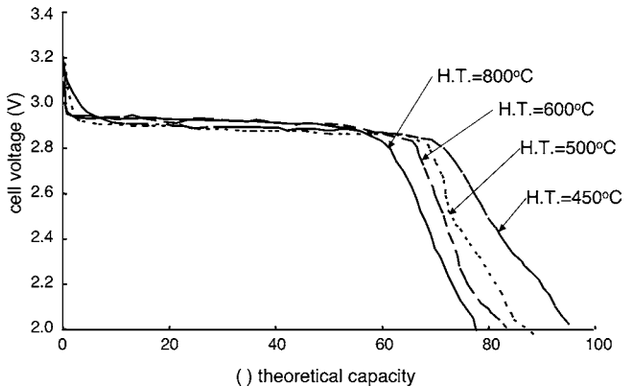

Figure 8. Experimental discharge curves of Li/PEO-$LiClO_4$/$Li_{1+x}Mn_2O_4$ at *C*/10 (Ref. 49).

$$D_2 = H_R \frac{RT}{c_2 F^2} \kappa_2 \qquad [15]$$

where c_2 is the electrolyte concentration, and H_R is the Haven ratio which is defined as the ratio of the tracer diffusion coefficient to ionic conductivity dependent diffusion coefficient. The Haven ratio is a collective correlation factor that describes interparticle correlations. For oxide glasses and other ion-conducting solids, the Haven ratio is usually greater than one;[74] for an H_R of one, Eq. 15 reduces to the Nernst-Einstein equation. Although the Nernst-Einstein equation is unsuitable for single-ion or dual-ion polymer electrolyte[73,74] because of the coupling between ion transport and host mobility, the deviation of the estimation of diffusivity by the Nernst-Einstein equation is less than an order of magnitude from the estimate by the modified Nernst-Einstein equation in Eq. 15.[73] Hence, the ionic diffusivity of polymer electrolyte, PEO-$LiClO_4$ was approximated using Eq. 15 with an H_R of unity. Use of Eq. 15 could potentially be eliminated in future work, with accurate experiments to determine the ionic conductivity and diffusivity.

Two additional, fitted parameters were used. The first fitted parameter was the diffusivity of the cathode active material. As discussed in Ref. 49, the ionic diffusivities of active material varied with preparation temperature. The values of the ionic diffusivity for the positive active particles were chosen such that the discharge curve of models with particle sizes of 3.6 μm in regular arrays fit the experimental results of Ref. 49 as shown in Fig. 8. Next, the same diffusivities were used for models using different particle sizes and microstructures, but with identical sintering temperatures. The second fitted parameter was the contact resistance, R_c, at the interface between the positive active particles and the positive current collector, which was adjusted to match the experimental results as in Fig. 8 as well.

Next, the "Comsol multiphysics solver" was used to analyze the 3D finite element model. The "Direct (UMFPACK)" time-dependent solver was used for this study. This type of solver is highly efficient for nonsymmetric systems.[52] The time evolution of the electrochemical field was calculated by setting up a time step of 100 s. The tolerance for convergence was chosen such that "relative tolerance" was set to be 0.001, and the "absolute tolerance" was set to be 0.0001. Generally, the relative error is less than the relative tolerance if the solution is large, and the absolute error is less than the absolute tolerance for the corresponding solution component if the solution is small. Other settings were the default values used by the Comsol solver.

Results

Electrochemical performance of the porous cathode electrode.— Simulation results of Fig. 9 and 10 show concentration contours of Li ions in the positive active particles, and illustrate that the concentration of Li ions in each particle were concentrically distributed, increasing from the core toward the surface, regardless of particle arrangement. Figure 11 shows the history of concentration of Li ions along the centerline of the unit volume of the 3D model with regularly packed $Li_{1+x}Mn_2O_4$ particles, of 6 μm diameter and sintering at 800°C. The concentration of Li ions near the current collector of positive electrode was lower than that on the electrolyte side; further, the concentration of Li ions was higher at the surface of each particle than within the core, as shown by Fig. 9 and 10.

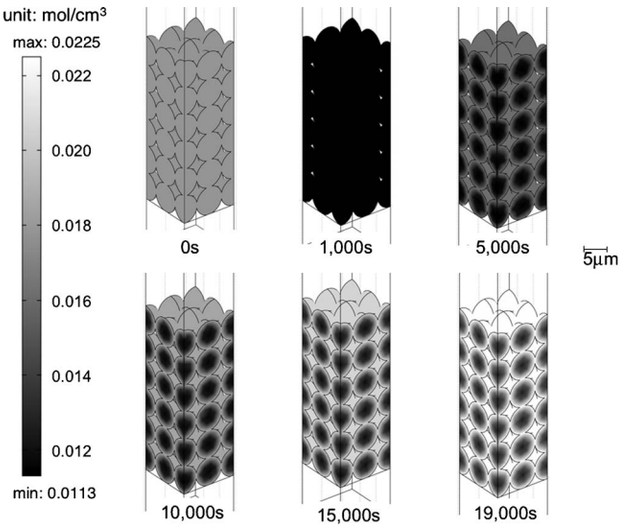

Figure 9. Simulation results for Li-ion concentration in the cathode particulate network at different simulation times (0, 1000, 5000, 10,000, 15,000, and 19,000 s), 6 μm particles, sintered at 800°C, and arranged in a regular array of a Li/PEO-$LiClO_4$/$Li_{1+x}Mn_2O_4$ cell, discharged at *C*/10, between 3.2 and 2.0 V.

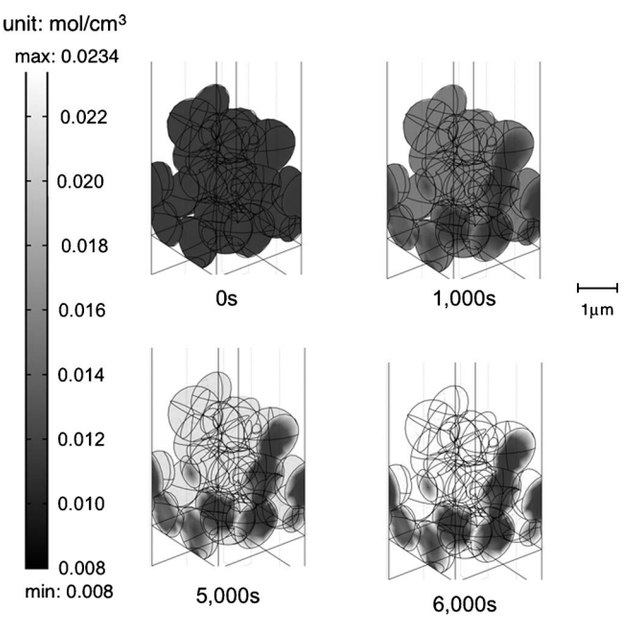

Figure 10. Simulation results for Li-ion concentration in the cathode particulate network at different simulation times (0,1000, 5000, and 6000 s) for 12 μm particles, sintered at 800°C, and arranged randomly in Li/PEO-$LiClO_4$/$Li_{1+x}Mn_2O_4$ cell, discharged at *C*/10, between 3.2 and 2.0 V.

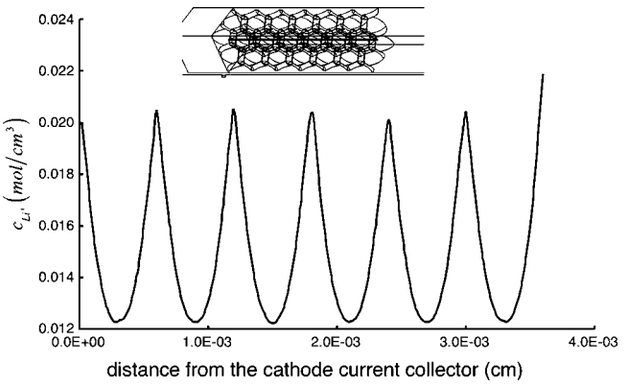

Figure 11. Li-ion concentration in cathode active particles along the centerline (as indicated in top corner of the model image) for a regularly arrayed cathode particulate network, with 6 μm particles and sintering at 800°C, as the cell discharged to 2 V.

The saturation of the Li ions concentration in the particles of positive electrode can be used as an indication of how well the Li ions have been intercalated into the positive electrode network, with degree of saturation defined as

$$\text{saturation} = \frac{c_{\text{Li}^+}^{\text{inner}} - c_s}{c_s^{\max} - c_s} \quad [16]$$

where $c_{\text{Li}^+}^{\text{inner}}$ is the Li ion concentration at $r = 0$ of a particle in the positive electrode at a discharge voltage of 2.0 V; c_s and $c_s^{\max}$ are the initial ($x = 0$) and maximum allowable ($x = 1$) Li ion concentrations, respectively, of $Li_{1+x}Mn_2O_4$ particles. The degree of saturation ranges from 0 to 1, for concentrations of Li ions ranging from c_s to $c_s^{\max}$. The ideal degree of saturation is unity.

Figure 12 shows that the degree of saturation dropped with increasing particle size. Saturation reached about 95% for 3.6 μm particles heat-treated at 450°C. However, the saturation became negative for 12 μm particles, for heat treatments greater than 500 and 600°C, in random and regular arrays, respectively. This aphysical result of a negative saturation stemmed from low diffusivity and large particle sizes: Li ions in the inner core actually must diffuse to the outer surface, to maintain electriconeutrality.

Structural randomness further impedes ionic migration of particles of higher ionic diffusivity. Although the average saturation of a random network structure was higher than that for a regular array, as diffusivity was reduced, the behaviors of these cathodes became similar. Thus, the smallest of the sizes studied (6 μm) was preferred, among all cases studied (6–12 μm).

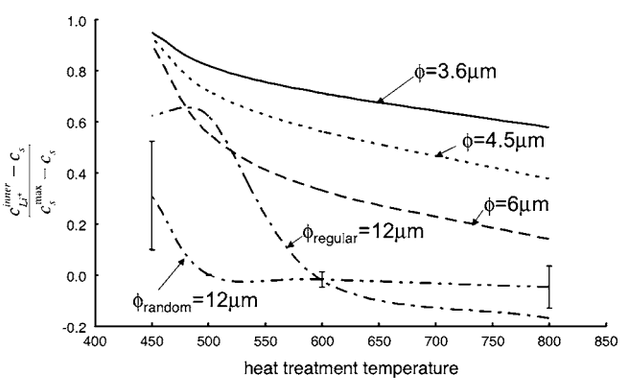

Figure 12. Saturation curves for particles, as defined in Eq. 16, for different sizes and sintering temperatures.

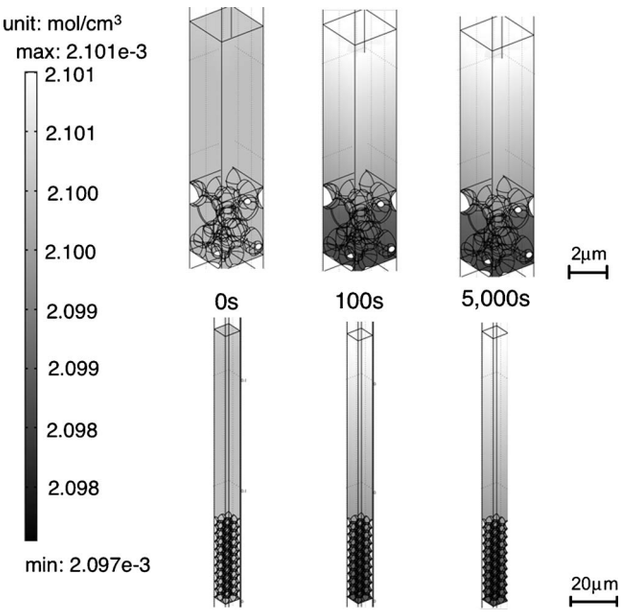

Figure 13. Simulation results for Li-ion concentration distribution in the electrolyte phase of a Li/PEO-$LiClO_4$/$Li_{1+x}Mn_2O_4$ cell, discharged at *C*/10 rate between 3.2 and 2.0 V, at different simulation times (0, 100, and 5000 s). Two different particle sizes and microstructures were simulated, as shown in two rows: particle sizes of 12 μm in random arrays, in the first row, and particle sizes of 3.6 mm in regular arrays, in the second row.

The concentration contour of Li ions in polymer electrolyte is a measure of the efficiency of the mass transport of mobile ions. Initially, the electrochemical potential difference drives migration of mobile ionic species between the two electrodes. A concentration gradient of ionic species is induced by this process, which ultimately reaches steady state. Simulation results here showed that as the Li-polymer cell was discharged at *C*/10, the concentration of Li ion in the electrolyte reached a steady state within 100 s, throughout the depth of the electrolyte, as shown in Fig. 13.

Validation of the computational algorithm.— Experimental results[49] were used to validate the proposed modeling technique. In Fig. 8, the experimental discharge curves of the second cycle for different sintering temperatures are summarized; they were used to estimate the Li ion diffusivity, the contact resistance, and to determine the impact of active particle size and arrangement on the cell performance.

Two parameters, Li-ion diffusivity into $Li_{1+x}Mn_2O_4$ particles, and contact resistance at the interface between the positive (cathode) particles and the current collector, were obtained by curve fitting the discharge curves of simulation results of regular array models, with $Li_{1+x}Mn_2O_4$ particles (3.6 μm) to experimental results. In Fig. 14-17, the discharge curves of model results of regular arrays with $Li_{1+x}Mn_2O_4$ particles (3.6 μm) were fitted with experimental values, for sintering temperatures of 800, 600, 500 and 450°C, under a constant, *C*/10 rate of discharge. The diffusivities of Li ion were found to be 4×10^{-13}, 6×10^{-13}, 1×10^{-12}, and 5×10^{-12} cm^2/s for $Li_{1+x}Mn_2O_4$ particles sintering at 800, 600, 500 and 450°C, respectively. Contact resistances were found to be 3.5 Ω cm^2 for $Li_{1+x}Mn_2O_4$ particles prepared at 600 and 800°C, and 10.5 Ω cm^2 for particles prepared at 450 and 500°C.

Prediction of discharge performance for various cathode architectures.— Figures 14-17 show prediction of the discharge performance of Li-polymer cells for different cathode architectures and particle sizes for $Li_{1+x}Mn_2O_4$ particles, sintered at various tempera-

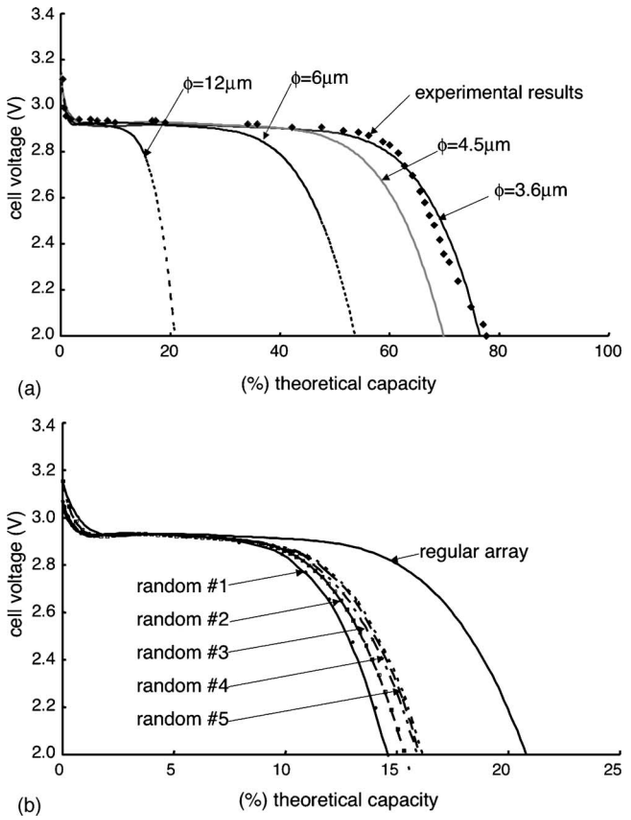

Figure 14. Galvanostatic discharge curves of cell voltages vs the fractional theoretical capacities of $Li_{1+x}Mn_2O_4$, for Li/PEO-$LiClO_4$/$Li_{1+x}Mn_2O_4$ discharged at $C/10$; $Li_{1+x}Mn_2O_4$ particles were prepared at 800°C. Comparisons include (a) simulated vs experimental results of Ref. 49 (in discrete diamonds, ◆) and calculated voltages (in solid and dashed lines) of the cell with four $Li_{1+x}Mn_2O_4$ particle sizes (3.6, 4.5, 6, and 12 μm) arranged in regular arrays; (b) calculated voltages of regular arrays (in black solid lines) and five different random arrays (in dashed lines) with $Li_{1+x}Mn_2O_4$ 12 μm particles.

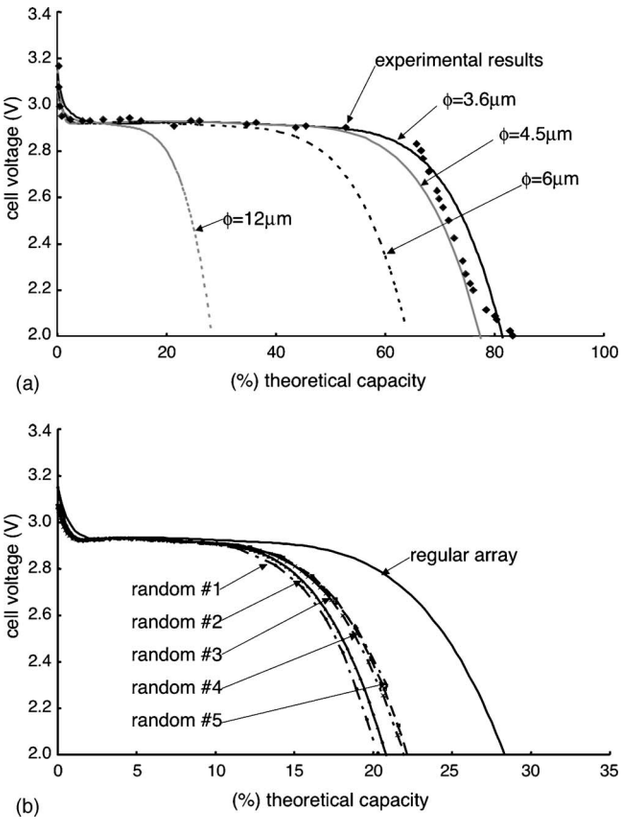

Figure 15. Galvanostatic discharge curves of cell voltages vs the fractional theoretical capacities of $Li_{1+x}Mn_2O_4$, for Li/PEO-$LiClO_4$/$Li_{1+x}Mn_2O_4$ discharged at $C/10$; $Li_{1+x}Mn_2O_4$ particles were prepared at 600°C. Comparisons include (a) simulated vs experimental results of Ref. 49 (in discrete diamonds, ◆) and calculated voltages (in solid and dashed lines) of the cell with four $Li_{1+x}Mn_2O_4$ particle sizes (3.6, 4.5, 6, and 12 μm) arranged in regular arrays; (b) calculated voltages of regular arrays (in black solid lines) and five different random arrays (in dashed lines) with $Li_{1+x}Mn_2O_4$ 12 μm particles.

tures. In each case, increasing particle size (3.6–12 μm) reduced achievable capacities significantly, as did randomness in packing.

Discussion

Validation of the computational algorithm.— Discrepancies between experimental and simulation results for cell discharge curves increase with increasing sintering temperature of cathode active particles. These discrepancies may be due to defects in $Li_xMn_2O_4$ spinel, since a second manganese oxide phase, Mn_2O_3, was detected in samples prepared at lower temperatures.[49] Further, the open-circuit potential used in current model was based on the crystalline structure of $LiMn_2O_4$. Hence, discrepancies between simulation and experimental results could be expected to increase as the $Li_{1+x}Mn_2O_4$ sintering temperature decreased, because of altered ionic and electronic kinetic properties, as shown previously.[75]

The first of two fitted parameters used in this proposed modeling strategy, diffusivity of $Li_{1+x}Mn_2O_4$, was determined to be 4×10^{-13}, 6×10^{-13}, 1×10^{-12}, and 5×10^{-12} cm^2/s for particles sintered at 800, 600, 500, and 450°C, respectively. This finding is consistent with an earlier hypothesis[49] that the mobility of Li ion is higher due to the defect $Li_xMn_{2-z}O_4$ spinel in the stoichiometric $LiMn_2O_4$ as the cathode particles prepared at lower sintering temperature, and is also consistent with an experimental finding[75] that the trend of diffusivity in samples sintered at 450°C is higher than for those sintered at 1100°C. These values are approximately three orders of magnitude smaller than the published diffusivities of 4.9×10^{-9}, 6.0×10^{-10} cm^2/s for samples sintering at 450°C and 1100°C, respectively,[75] which were obtained via the galvanostatic intermittent titration technique,[76] or 1×10^{-10}–2×10^{-9} cm^2/s as degree of insertion increased for samples heated at 800°C,[77] which were obtained via electrochemical voltage spectroscopy technique proposed by in Ref. 78.

In general, reported diffusivities of $Li_xMn_2O_4$ (where $0 < x < 1$) range widely, from 10^{-15} [79] to 2.6×10^{-8} [80] cm^2/s. These dissimilarities may be attributed to preparation conditions and experimental techniques.[28] Some experiments employ porous electrodes with added carbons for electrical conductivity; interactions between these additives and electrolyte may affect the diffusivity for Li ions in $Li_xMn_2O_4$.[81] Similar difficulties arise in characterization of diffusivity of Li ions in $Li_{1+x}Mn_2O_4$ samples. Though both fitted values of diffusivity for $Li_xMn_2O_4$ obtained by Ref. 28, 2.8×10^{-13} cm^2/s and the experimental results, 1.23×10^{-12}–1.55×10^{-12} cm^2/s obtained by potential step chronoamperometry method, of Ref. 82 on thin film $Li_xMn_2O_4$ are close to what were used in this study, the central trend of experimental results[82] contradicts the findings of the present study and other work.[75] Both showed that diffusivity increased as the annealing temperature increased from 400°C to its highest value of around 700°C. The diffusivity of $Li_{1+x}Mn_2O_4$ fitted in this study was independent from the degree of Li^+ insertion, x, unlike other experimental studies on x-dependent diffusivity.[77,79,80]

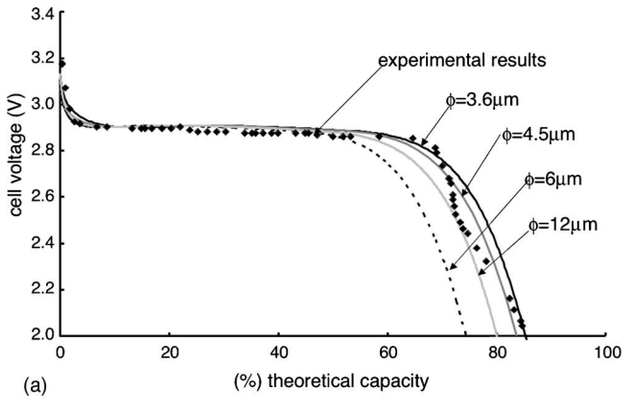

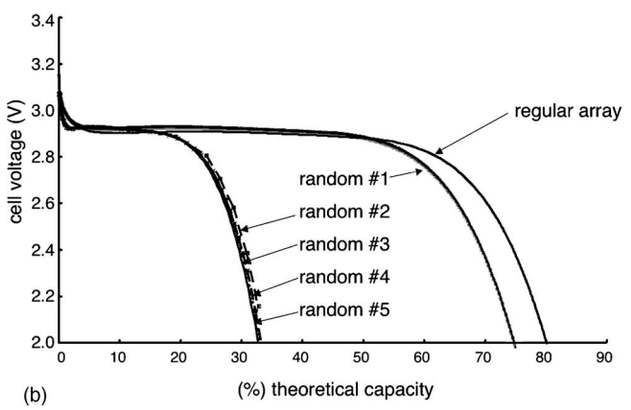

Figure 16. Galvanostatic discharge curves of cell voltages vs fractional theoretical capacities of $Li_{1+x}Mn_2O_4$, for Li/PEO-$LiClO_4$/$Li_{1+x}Mn_2O_4$ discharged at *C*/10; $Li_{1+x}Mn_2O_4$ particles were prepared at 500°C. Comparisons include (a) simulated vs experimental results of Ref. 49 (in discrete diamonds, ♦) and calculated voltages (in solid and dashed lines) of the cell with four $Li_{1+x}Mn_2O_4$ particle sizes (3.6, 4.5, 6, and 12 μm) arranged in regular arrays; (b) calculated voltages of regular arrays (in black solid lines) and five different random arrays (in dashed lines) with $Li_{1+x}Mn_2O_4$ 12 μm particles.

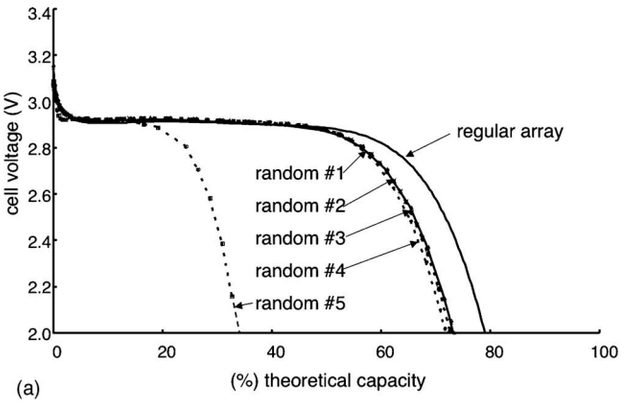

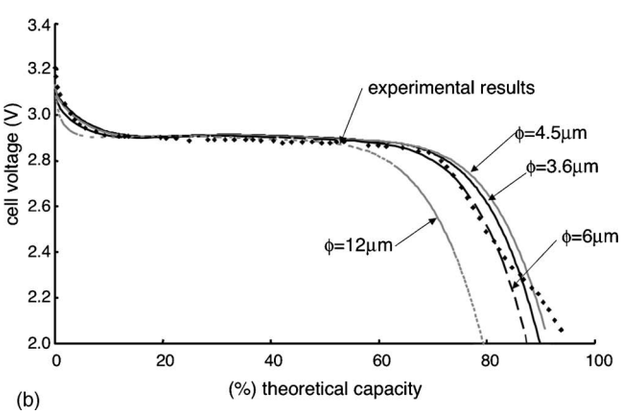

Figure 17. Galvanostatic discharge curves of cell voltages vs the fractional theoretical capacities of $Li_{1+x}Mn_2O_4$, for Li/PEO-$LiClO_4$/$Li_{1+x}Mn_2O_4$ discharged at *C*/10; $Li_{1+x}Mn_2O_4$ particles were prepared at 450°C. Comparisons include (a) simulated vs experimental results of Ref. 49 (in discrete diamonds, ♦) and calculated voltages (in solid and dashed lines) of the cell with four $Li_{1+x}Mn_2O_4$ particle size (3.6, 4.5, 6, and 12 μm) arranged in regular arrays; (b) calculated voltages of regular arrays (in black solid lines) and five different random arrays (in dashed lines) with $Li_{1+x}Mn_2O_4$ 12 μm particles.

The second fitted parameter, contact resistance, was lower for the higher sintering temperature, as shown in Table I. This was based on analysis of the cell voltage curves, in which the nominal cell voltage was higher for higher sintering temperatures, as shown in Fig. 8. These fitted values were much smaller than the one used in Ref. 83. The value of contact resistance depended upon the size of the particles, conductivity of the adjacent particles, and pressure applied during manufacturing.[84]

The regular array model results were directly compared with a classic continuum model, by continuum simulations[85] and a modified one-dimensional (1D) Comsol model.[86] The values of all parameters used for the classic continuum model and the modified 1D Comsol model were identical to those listed in Table I. Figure 18 shows the comparisons among the results obtained by the 1D Fortran, the modified 1D Comsol, present 3D finite element models, and the experimental result of particle sintering at 450°C. In these models, the particle size was 6 μm. Based on this result, we were confident that the differences between the 1D and 3D models presented later are not due to the solver issue and dimensionality. Figures 19a and b show results for samples sintering at 450 and 800°C, respectively. The difference in achievable capacities at a *C*/10 discharge rate between the current model and the prior 1D Fortran model[85] for the active material samples sintering at 450°C was within 5% for particles smaller than 6 μm, but approximately 15% for particle sizes of 12 μm, as shown in Fig. 19a. The difference for the active material samples sintered at 800°C became larger, with the difference increasing from 16 to 50% as particle sizes increased from 3.6 to 12 μm, as shown in Fig. 19b. However, trends for cell voltage and achievable capacity at a *C*/10 discharge rate for both cases were similar. The increased difference between two models, for particles sintered at 450°C and 12 μm in diameter, could be due to a breakdown of the effective medium theory, implemented as the Bruggeman equation, because the total thickness of the cathode was around 36 μm, or three times the diameter of the particle. For the low diffusivity cases shown in Fig. 19b, the source of the large difference between the two models was less clear. It is possible that diffusion paths in the regular array models were less resistant than assumed by the averaging technique.

Electrochemical performance of a porous cathode electrode.— Overall, the model results showed that the distribution of Li ion concentration in $Li_{1+x}Mn_2O_4$ particles was a function of particle arrangements, particle sizes, Li ions diffusivity, electrons conductivity, and time. In Fig. 12, the saturation curves of the $Li_{1+x}Mn_2O_4$ particulate networks showed that smaller particles show a higher degree of saturation, which implies that the Li ions reach the core of each particle faster. The $Li_{1+x}Mn_2O_4$ particles sintered at 450°C could intercalate to about 95, 92, 90, and 62% for particle sizes of 3.6, 4.5, 6, and 12 μm, respectively. But the degree of saturation for $Li_{1+x}Mn_2O_4$ particles of 3.6, 4.5, 6, and 12 μm was only 57, 37, 14, and −5%, respectively, as the sintering temperature increased to 800°C. For the particle sizes of 12 μm, the initial concentration of

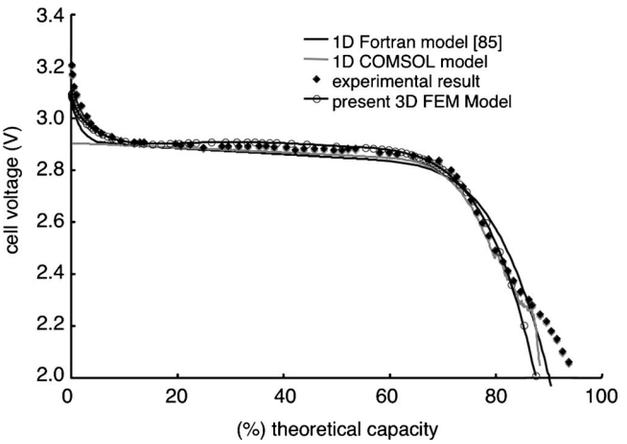

Figure 18. Comparisons of calculated galvanostatic discharge curves of Li/PEO-$LiClO_4$/$Li_{1+x}Mn_2O_4$ cell, with $Li_{1+x}Mn_2O_4$ particle size of 6 μm, prepared at 450°C, for the three different simulation models. Values were obtained by running the 1D Fortran program (Ref. 85) (in solid black line), by the modified 1D Comsol model as Ref. 86 (in solid gray line), by the current approach using regular microstructures (in solid black line with white circle). The discrete diamonds, ♦, are experimental results.

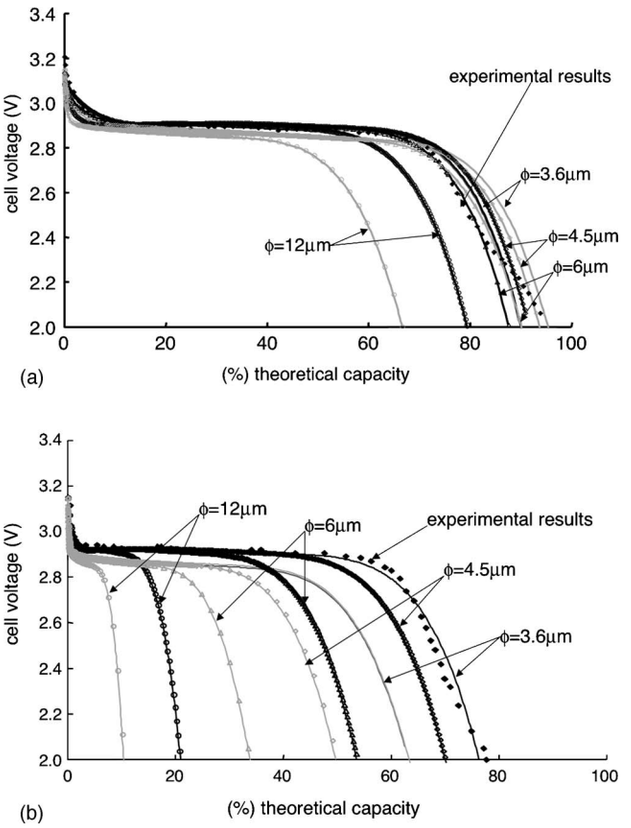

Figure 19. Comparisons of calculated galvanostatic discharge curves of Li/PEO-$LiClO_4$/$Li_{1+x}Mn_2O_4$ cell, with four different $Li_{1+x}Mn_2O_4$ particle sizes, prepared at two temperatures, (a) 450°C and (b) 800°C, respectively. Values were obtained by the finite element approach, using regular microstructures, and by running the 1D Fortran program (Ref. 85). Darker and lighter lines are the calculated discharge curves obtained by current approach, and by the program developed previously (Ref. 85), respectively. The discrete diamonds, ♦, are experimental results. The solid lines without symbols, with white diamonds, ◇, with white triangles, △, and with white circles, ○, represent particle size of 3.6, 4.5, 6.0, and 12.0 μm, respectively.

Li ions had to be transported from the core toward the surface of $Li_{1+x}Mn_2O_4$ particles, to maintain electroneutrality; therefore, the degree of saturation became negative.

The electronic conductivity of $Li_{1+x}Mn_2O_4$ particles strongly affects cell performance. For high electronic conductivity, lithium insertion initiates in particles at the top surface of the cathode particulate network, closer to the lithium metal, as shown in Fig. 12. The fast motion of electrons compensates for this Li ion intercalation. Conversely, for low electronic conductivity, the insertion process would initiate with particles on the Ni metal current collector side. The slow motion of electrons cannot counterbalance Li ion intercalation at the top surface of the $Li_{1+x}Mn_2O_4$ particulate network; hence, the insertion initiates on the side where electrons are available.

Figures 14a, 15a, 16a, and 17a show the effect of particle size on the discharge performance of Li/PEO-$LiClO_4$/$Li_{1+x}Mn_2O_4$ cell at a *C*/10 rate, without consideration of the arrangement of the particles. These figures collectively demonstrated that smaller particle sizes are preferable for high power density applications, because of the high achievable capacity under the same rates. The differences among achievable capacities between 3.6 and 12 μm of $Li_{1+x}Mn_2O_4$ particles reduces from 60 to 10% of theoretical capacity, as diffusivity increases from 4×10^{-13} to 5×10^{-12} cm^2/s.

However, the smaller particle sizes do not always assure higher achievable capacities, as shown in Fig. 16a and 17a; 12 μm particles showed higher achievable capacity than 6 μm, one by about 5% of the theoretical capacity, for a particle sintering temperature 500°C, corresponding to the diffusivity of 1×10^{-12} cm^2/s. Similarly, the achievable capacity of 4.5 μm particle is larger than that for a 3.6 μm particle by about 1% of the theoretical capacity. Thus, we see that a smaller particle size is preferable when the diffusivity of $Li_{1+x}Mn_2O_4$ is low, but the difference is reduced with increasing diffusivity.

Figures 14b, 15b, 16b, and 17b show the impact of the microstructure of $Li_{1+x}Mn_2O_4$ network on the discharge performance of Li/PEO-$LiClO_4$/$Li_{1+x}Mn_2O_4$ cell under *C*/10 rate without consideration of particle size. They demonstrate that the regular array of the $Li_{1+x}Mn_2O_4$ network is always superior to the random arrays of $Li_{1+x}Mn_2O_4$ networks, because of their higher achievable capacities. However, the differences among achievable capacities among the regular arrays and random arrays models is reduced, as diffusivities of $Li_{1+x}Mn_2O_4$ increase. The exception to this is for particles of diffusivity 1×10^{-12} cm^2/s, corresponding to a cathode particle sintering temperature of 500°C. The results also show that the variation among random models for the achievable capacity increases from 1.5%, 2%, 43%, and 40% of the theoretical capacity, calculated relative to the random model with the highest achievable capacity, as $Li_{1+x}Mn_2O_4$ diffusivities increase from 4×10^{-13}, 6×10^{-13}, 1×10^{-12}, to 5×10^{-12} cm^2/s, respectively. These differences among the achievable capacities obtained by the regular array model and the random array model could be due to the intrinsically higher tortuosity. Though regular arrays may not be merited, based on their obviously higher cost, they produce a measurably better capacity.

Spinel $LiMn_2O_4$ is a promising cathode material because of its low cost, excellent voltage profile and its low environmental impact, but instability has limited its usage. Increasing sintering temperature affects cyclability and capacity retention of spinel $Li_{1+x}Mn_2O_4$, by suppressing Jahn-Teller distortion, i.e., the geometric distortion arising in nonlinear molecules to remove a degeneracy in the electronic ground state. Improvements to rechargeability and electrical conductivity have also been made by variation of the metal–oxygen bond lengths in the structure, by increasing sintering or annealing temperatures during preparation.[75,82]

To date, PEO has been the most studied polymer electrolyte. Ionic conduction of the PEO-$LiClO_4$ polymer electrolyte is closely associated with the local segmental motion of the PEO polymer. The high crystallinity of polymer electrolytes in general, of ~85%,[87]

inhibits ionic conduction. Because PEO polymer melts at ~65°C,[87] it is common to operate PEO-host polymer electrolytes at high temperature, to increase ionic conductivity. The ionic conductivity of PEO-$LiClO_4$ electrolyte operation at 120°C was set to be 3.8×10^{-3} S/cm for the models studied here, which is comparable to most lithium polymer electrolytes such as 1×10^{-3} S/cm for $LiClO_4$-EC-PC-PAN, 3.9×10^{-3} S/cm for $LiClO_4$-EC-DEC-PAN as in Ref. 88, but slightly lower than that for liquid electrolytes, which have ionic conductivities of $\sim 1 \times 10^{-3}$–1×10^{-2} S/cm[89] at ambient temperature.

For the PEO-$LiClO_4$ electrolyte, the key properties that determine ionic transport species are the diffusivities and transference numbers of the corresponding species, when the electrochemical stability of PEO-$LiClO_4$ polymer electrolyte is neglected. The simulation results of Fig. 13 show that the microstructure of the positive electrode does not affect transport of the ionic species in the PEO-$LiClO_4$ polymer electrolyte at a $C/10$ discharge rate.

Comparison with other techniques.— The porous electrode[25-29,83] and two-dimensional (2D) finite element[10] approaches share similar focus on the effects of materials on cell function and governing equations. However, the porous electrode theory, though computationally efficient, does not consider the impact of the microstructure of the electrode in the detail presented here. This study shows that the microstructure of the lithium ion cell significantly affects achievable capacity, beyond its porosity; the arrangements of particles have a strong and quantifiable effect on performance.

Two-dimensional finite element approaches have not, as yet, considered the microstructure of the electrode, but instead relied upon somewhat less realistic, symmetric microstructural assumptions.[10] Equivalent-circuit models,[30-40] generally interested in cell impedance, have also been used to simulate the cell voltage and rate performance.[33] Models in this class generally generate similar results to experimental values because of their empirical nature, but are unable to predict the effects of particle shape, sizes and arrangements. First-principles approaches[41-44] provide excellent guidance in the selection of candidate active materials, but they are not as yet scalable, given their computational intensity, to models of microstructure.

Though a "shrinking core" model has been proposed to model the radius-dependent two-phase discharge process for NiMH[90-92] and $LiFePO_4$,[93,94] it may not be wholly suitable for the present work, in light of recent results. $LiFePO_4$, for example, has two phases ($FePO_4$ and $LiFePO_4$) during Li insertion, as does $Li_{1+x}Mn_2O_4$ ($LiMn_2O_4$ and $Li_2Mn_2O_4$); the former system has been modeled as a solid solution of $Li_{1-\varepsilon}FePO_4$ as a growing shell surrounding the core of solid solution of $Li_\delta FePO_4$ with Li ion insertion.[94] Recent experiments,[95-97] however, have called into question the characterization of this system as a solid solution. The preferential location of $FePO_4$ in the core region of particles and $LiFePO_4$ at the surfaces has been recently attributed to a one-dimensional growth mechanism,[95,96] rather than a core-shell (three-dimensional) growth pattern.[97] To date, the shrinking core model has not been used to characterize or model the spinel $LiMn_2O_4$ system, although in the tetragonal system, which is similar to the $LiFePO_4$ system, $Li_2Mn_2O_4$[98] has been observed to grow from the surface of active particles to the bulk $LiMn_2O_4$.

Single-phase diffusion models thus appear proper at present, for modeling the insertion of Li ions to $Li_{1+x}Mn_2O_4$. First, the diffusion coefficient used is an average value, accounting for two-phase mechanisms. Second, the diffusion model is consistent with both observations, and classic models. Specifically, Li ions of $Li_2Mn_2O_4$ initially inserted at the surface of a particle during the discharge process must hop toward the core[95] for $LiFePO_4$; otherwise, the insertion process is terminated, as shown by the Butler-Volmer equations (Eq. 3 and 6), once $Li_2Mn_2O_4$ concentration is saturated at the surface region. Hence, Li ions are shared between the $LiMn_2O_4$ and $Li_2Mn_2O_4$ phases, in the region between the surface and core. Their concentration profiles should thus increase, from the core toward the edge of a particle during discharge. Also, the simulation results[99] based on single-phase diffusion mechanism for ellipsoidal particles have shown that higher concentrations occur in the tip region of the ellipsoidal particle during insertion. Similar experimental results have shown a higher probability of observation of pure $Li_2Mn_2O_4$[98] or $LiFePO_4$[96] in the small curvature surface region of a particle during the discharge process, which is indicative of higher Li-ion concentration in those regions.

Conclusion

Our 3D finite element model scheme has been demonstrated to be a design tool for prediction of performance of an electrochemical cell. This scheme incorporates the microstructure of the whole cell, and physics-based governing and boundary equations, to predict the cell performance. More advanced kinetic characterization and interfacial interactions can be readily included in the governing or boundary equations.

Based on results here, we have shown that the microstructure of the electrode is critical to performance. Though impractical at present, given current manufacturing techniques, regular arrays were shown to increase achievable capacity about 5–50% of the theoretical capacity compared with random arrays, at $C/10$ for samples sintered at 500°C. Smaller particle sizes of active material particles were also shown to be beneficial for high power density applications, for low diffusivity of active materials. For example, the achievable capacity increased from 20 to 75% as the particle size decreased from 12 to 3.6 μm for the active particles sintered at 800°C, as shown in Fig. 14a. The microstructure of the active material does not impact electrolyte performance, as demonstrated in Fig. 13, which shows that Li^+ concentration is not dependent on the particle size and microstructure over time.

There are some challenges to implementation of the scheme proposed for more complex cells. First, the high intrinsic computational intensiveness of the methods here prohibits simulation domains of significant size relative to cell size, at present. Approximately 2–4 hours of run time were required for each model in this study, which each comprised about 10,000–25,000 meshes, on a Dell OptiPlex GX 620 with 3.4 GHz CPU and 2 GBit RAM. More meshes would be required for a cell comprised of two porous random-structure electrodes and a separator. Second, this scheme requires some experimentation to determine key kinetic parameters in the particle scale, including ionic diffusivity and conductivity of the electrolyte, and ionic diffusivity and electron conductivity of the active material particles.

One element of future work will be to consider the stresses inside and among the active particles, due to Li^+ intercalation[31] and compression during manufacturing of cells, in order to analyze possible failure mechanisms. Also, inclusion of contact among particles will be needed to achieve a more complete understanding of the effects of high surface area, trade-offs between power performance and impedance losses. Verification of the model experimentally, in other systems, will also be part of future work.

Acknowledgments

Support for this project provided by the Army Research Office (Dr. Bruce LaMattina, Program Manager), Ford Motor Company (Ted Miller and Kent Snyder, Program Managers) and the BATT Program of the Department of Energy (Dr. Tien Duong) is gratefully acknowledged.

University of Michigan assisted in meeting the publication costs of this article.

Appendix

The Nernst-Planck equations included in the Comsol multiphysics package (version 3.2) were used for this computational model. The governing assumptions of mass balance, electrical neutrality, and concentrated solution theory are followed, since conservation of mass is required, under conditions of high salt concentration.

As discussed in Ref. 55, the flux of binary ionic species for concentrated solution is governed by the gradient of the electrochemical potential, μ_2 as

$$\mathbf{N}_+ = -\frac{\nu_+ \mathcal{D}_2}{\nu RT}\frac{c_T}{c_0} c \nabla \mu_2 + \frac{\mathbf{i} t_+^0}{z_+ F} + c_+ v_0$$

$$\mathbf{N}_- = -\frac{\nu_- \mathcal{D}_2}{\nu RT}\frac{c_T}{c_0} c \nabla \mu_2 + \frac{\mathbf{i} t_-^0}{z_- F} + c_- v_0 \quad [A\text{-}1]$$

where $\mathcal{D}_2$, is the diffusion coefficient of the electrolyte, c_T is the total concentration; μ_2 can be expressed in terms of mean molar activity coefficient, $f_\pm$, and the proportional constant, $a_\pm^\theta$, as

$$\mu_2 = \nu RT \ln c f_\pm a_\pm^\theta \quad [A\text{-}2]$$

The current density in Eq. 17 is defined as

$$\mathbf{i} = F\sum_i z_i \mathbf{N}_i = F z_+ \mathbf{N}_+ + F z_- \mathbf{N}_- \quad [A\text{-}3]$$

The current density can be expressed in terms of the salt concentration gradient, mean molar activity coefficient, conductivity and electrical potential of the electrolyte[58] as

$$\mathbf{i} = -\kappa_2 \nabla \Phi_2 + \kappa_2 \frac{2RT}{cF}\left(1 + \frac{d \ln f_\pm}{d \ln c}\right)(1 - t_+^0) \nabla c \quad [A\text{-}4]$$

Then the flux equation listed at Eq. 17 can be rearranged as

$$\begin{aligned}\mathbf{N}_i &= -\nu_i \mathcal{D}_2 \frac{c_T}{c_0}\left[1 + \frac{d \ln f_\pm}{d \ln c}\right] \nabla c + \frac{\mathbf{i} t_i^0}{z_i F} + c_i \mathbf{v}_0 \\ &= -\nu_i \mathcal{D}_2 \frac{c_T}{c_0}\left[1 + \frac{d \ln f_\pm}{d \ln c}\right] \nabla c + \frac{2\kappa_2 t_i^0 RT}{c z_i F^2}\left(1 + \frac{d \ln f_\pm}{d \ln c}\right)(1 - t_+^0) \nabla c - \frac{\kappa_2 t_i^0}{z_i F} \nabla \Phi_2 \\ &\quad + c_i \mathbf{v}_0 \\ &= \left[-\nu_i \mathcal{D}_2 \frac{c_T}{c_0} + \frac{2(1 - t_+^0)\kappa_2 t_i^0 RT}{c z_i F^2}\right]\left(1 + \frac{d \ln f_\pm}{d \ln c}\right) \nabla c - \frac{\kappa_2 t_i^0}{z_i F} \nabla \Phi_2 + c_i \mathbf{v}_0 \end{aligned} \quad [A\text{-}5]$$

Hence, for binary electrolyte

$$\mathbf{N}_+ = \left[-\nu_+ \mathcal{D}_2 \frac{c_T}{c_0} + \frac{2\kappa_2 t_-^0 t_+^0 RT}{c_+ z_+ F^2}\right]\left(1 + \frac{d \ln f_\pm}{d \ln c}\right) \nabla c_+ - \frac{\kappa_2 t_+^0}{z_+ F} \nabla \Phi_2 + c_+ \mathbf{v}_0$$

$$\mathbf{N}_- = \left[-\nu_- \mathcal{D}_2 \frac{c_T}{c_0} + \frac{2\kappa_2 t_-^{02} RT}{c_- z_- F^2}\right]\left(1 + \frac{d \ln f_\pm}{d \ln c}\right) \nabla c_- - \frac{\kappa_2 t_-^0}{z_- F} \nabla \Phi_2 + c_- \mathbf{v}_0 \quad [A\text{-}6]$$

In Comsol's "Chemical Engineering Module," the Nernst-Planck equations, which would take into account the electrical neutrality, and mass balance directly, have the same form as Eq. 19. Hence, it can implement into Comsol with proper coefficients.

If solvent velocity, $\mathbf{v}_0$, is small to neglect, Eq. 11 could be simplified as

$$\mathbf{N}_+ = \left[-\nu_+ \mathcal{D}_2 \frac{c_T}{c_0} + \frac{2\kappa_2 t_-^0 t_+^0 RT}{c_+ z_+ F^2}\right]\left(1 + \frac{d \ln f_\pm}{d \ln c}\right) \nabla c_+ - \frac{\kappa_2 t_+^0}{z_+ F} \nabla \Phi_2$$

$$\mathbf{N}_- = \left[-\nu_- \mathcal{D}_2 \frac{c_T}{c_0} + \frac{2\kappa_2 t_-^{02} RT}{c_- z_- F^2}\right]\left(1 + \frac{d \ln f_\pm}{d \ln c}\right) \nabla c_- - \frac{\kappa_2 t_-^0}{z_- F} \nabla \Phi_2 \quad [A\text{-}7]$$

List of Symbols

α_A, α_B	anodic and cathodic apparent transfer coefficients
ϕ	diameter of the cathode active material
Φ_2	electric potential of electrolyte
κ_2	ionic conductivity of PEO-$LiClO_4$ polymer electrolyte
κ_3	electronic conductivity of $Li_{1+x}Mn_2O_4$ particles
κ_1	electronic conductivity of lithium metal foil
κ_4	electronic conductivity of nickel metal foil
η	overpotential
v_+, v_-	numbers of cations and anions into which a molecule of electrolyte dissociates
c_0	electrolyte initial concentration
c_s	initial lithium concentration in $Li_{1+x}Mn_2O_4$
$c_3^{\max}$	maximum lithium concentration in $Li_{1+x}Mn_2O_4$ as y equaled to 1
$\mathcal{D}_2$	diffusivity of electrolyte
D_3	diffusivity of Li ion in $Li_{1+x}Mn_2O_4$
D_{ij}	pairwise interaction parameter between species i and j
f_m	mean molar activity coefficient of the salt
F	Faraday's constant
$\mathbf{I}$	current density
$i_{i,j}$	exchange current density at the interface of i and j phase
$\mathbf{N}_+, \mathbf{N}_-$	molar flux of positive and negative ions
R	gas constant
R_c	contact resistance at the interface of cathode particles and current collector
t	thickness of the cathode
t_+, t_-	transference numbers of positive and negative ions
T	working temperature
U	open-circuit potential
z_+, z_-	charge number of positive and negative ions

References

1. R. J. Gummow, A. Dekock, and M. M. Thackeray, *Solid State Ionics*, **69**, 69 (1994).
2. H. M. Wu, J. P. Tu, X. T. Chen, Y. Li, X. B. Zhao, and G. S. Cao, *J. Electroanal. Chem.*, **586**, 180 (2006).
3. A. K. Padhi, K. S. Nanjundaswamy, C. Masquelier, and J. B. Goodenough, *J. Electrochem. Soc.*, **144**, 2581 (1997).
4. C. H. Mi, X. G. Zhang, X. B. Zhao, and H. L. Li, *J. Alloys Compd.*, **424**, 327 (2006).
5. S.-W. Song, G. V. Zhuang, and P. N. Ross, Jr., *J. Electrochem. Soc.*, **151**, A1162 (2004).
6. I. Belharouak, D. Vissers, and K. Amine, *J. Electrochem. Soc.*, **153**, A2030 (2006).
7. Z. Lu and J. R. Dahn, *J. Electrochem. Soc.*, **148**, 237 (2001).
8. P. He, H. Wang, L. Qi, and T. Osaka, *J. Power Sources*, **160**, 627 (2006).
9. K. Zaghib, P. Charest, A. Guerfi, J. Shim, M. Perrier, and K. Striebel, *J. Power Sources*, **134**, 124 (2004).
10. R. E. Garcia, Y. M. Chiang, W. C. Carter, P. Limthongkul, and C. M. Bishop, *J. Electrochem. Soc.*, **152**, A255 (2005).
11. S. Torquato, *Random Heterogeneous Materials: Microstructure and Macroscopic Properties*, p. 10, Springer, New York (2002).
12. Y. B. Yi and A. M. Sastry, *Phys. Rev. E*, **66**, 066130 (2002).
13. Y. B. Yi and A. M. Sastry, *Proc. R. Soc. London, Ser. A*, **460**, 2353 (2004).
14. Y. B. Yi, C. W. Wang, and A. M. Sastry, *J. Electrochem. Soc.*, **151**, A1292 (2004).
15. C. W. Wang, Y. B. Yi, A. M. Sastry, J. Shim, and K. A. Striebel, *J. Electrochem. Soc.*, **151**, A1489 (2004).
16. Y. B. Yi, C. W. Wang, and A. M. Sastry, *J. Eng. Mater. Technol.*, **128**, 73 (2006).
17. S. Ahn, Y. Kim, K. J. Kim, T. H. Kim, H. Lee, and M. H. Kim, *J. Power Sources*, **82**, 896 (1999).
18. J. S. Sakamoto and B. Dunn, *J. Electrochem. Soc.*, **149**, A26 (2002).
19. K. Zaghib, J. Shim, A. Guerfi, P. Charest, and K. A. Striebel, *Electrochem. Solid-State Lett.*, **8**, A207 (2005).
20. C. M. Julien, K. Zaghib, A. Mauger, M. Massot, A. Massot, A. Ait-Salah, M. Selmane, and F. Gendron, *J. Appl. Phys.*, **100**, 063511 (2006).
21. Y.-H. Chen, C.-W. Wang, G. Liu, X.-Y. Song, V. S. Battaglia, and A. M. Sastry, *J. Electrochem. Soc.*, **154**, A978 (2007).
22. D. Guy, B. Lestriez, R. Bouchet, and D. Guyomard, *J. Electrochem. Soc.*, **153**, A679 (2006).
23. L. J. Fu, K. Endo, K. Sekine, T. Takamura, Y. P. Wu, and H. Q. Wu, *J. Power Sources*, **162**, 663 (2006).
24. M. Kise, S. Yoshioka, K. Hamano, H. Kuriki, T. Nishimura, and H. Urushibata, *J. Electrochem. Soc.*, **153**, A1004 (2006).
25. M. Doyle and J. Newman, *Electrochim. Acta*, **40**, 2191 (1995).
26. J. Newman, K. E. Thomas, H. Hafezi, and D. R. Wheeler, in *Modeling of Lithium-Ion Batteries*, Selected Papers Presented at the 11th IMLB, June 22–28 2002, p. 838, Elsevier, Monterey, CA (2003).
27. R. Darling and J. Newman, *J. Electrochem. Soc.*, **144**, 4201 (1997).
28. E. Deiss, D. Haringer, P. Novak, and O. Haas, *Electrochim. Acta*, **46**, 4185 (2001).
29. M. Doyle, J. Newman, A. S. Gozdz, C. N. Schmutz, and J. M. Tarascon, *J. Electrochem. Soc.*, **143**, 1890 (1996).
30. N. Ariel, G. Ceder, D. R. Sadoway, and E. A. Fitzgerald, *J. Appl. Phys.*, **98**, 023516 (2005).
31. Y. Zhang, Y. W. Liu, Y. S. Cheng, and X. G. Hu, *J. Central South Univ. Technol.*, **12**, 309 (2005).
32. B. Y. Liaw, R. G. Jungst, G. Nagasubramanian, H. L. Case, and D. H. Doughty, *J. Power Sources*, **140**, 157 (2005).
33. B. Y. Liaw, G. Nagasubramanian, R. G. Jungst, and D. H. Doughty, *Solid State Ionics*, **175**, 835 (2004).
34. S. Abu-Sharkh and D. Doerffel, *J. Power Sources*, **130**, 266 (2004).
35. E. Barsoukov, D. H. Kim, H. S. Lee, H. Lee, M. Yakovleva, Y. Gao, and J. F. Engel, *Solid State Ionics*, **161**, 19 (2003).
36. I. Bloom, S. A. Jones, E. G. Polzin, V. S. Battaglia, G. L. Henriksen, C. G. Motloch, R. B. Wright, R. G. Jungst, H. L. Case, and D. H. Doughty, *J. Power Sources*, **111**, 152 (2002).
37. Y. C. Chang, J. H. Jong, and G. T. K. Fey, *J. Electrochem. Soc.*, **147**, 2033 (2000).
38. C. R. Yang, J. Y. Song, Y. Y. Wang, and C. C. Wan, *J. Appl. Electrochem.*, **30**, 29 (1999).
39. S. R. Narayanan, D. H. Shen, S. Surampudi, A. I. Attia, and G. Halpert, *J. Electrochem. Soc.*, **140**, 1854 (1993).
40. D. C. Grahame, *J. Am. Chem. Soc.*, **68**, 301 (1946).
41. J. N. Reimers, *J. Power Sources*, **54**, 16 (1995).
42. C. Y. Ouyang, S. Q. Shi, Z. X. Wang, X. J. Huang, and L. Q. Chen, *Phys. Rev. B*, **69**, 104303 (2004).
43. K. Moriguchi, S. Munetoh, M. Abe, M. Yonemura, K. Kamei, A. Shintani, Y. Maehara, A. Omaru, and M. Nagamine, *J. Appl. Phys.*, **88**, 6369 (2000).
44. M. E. Garcia, E. Webb, and S. H. Garofalini, *J. Electrochem. Soc.*, **145**, 2155 (1998).
45. J. O. Besenhard, J. Yang, and M. Winter, *J. Power Sources*, **68**, 87 (1997).
46. A. Guerfi, P. Charest, K. Kinoshita, M. Perrier, and K. Zaghib, *J. Power Sources*, **126**, 163 (2004).
47. J. P. Cho and B. Park, *J. Power Sources*, **92**, 35 (2001).
48. K. Zaghib, G. Nadeau, and K. Kinoshita, *J. Electrochem. Soc.*, **147**, 2110 (2000).
49. W. J. Macklin, R. J. Neat, and R. J. Powell, *J. Power Sources*, **34**, 39 (1991).
50. M. M. Thackeray, *Prog. Solid State Chem.*, **25**, 1 (1997).

51. M. M. Thackeray, W. I. F. David, P. G. Bruce, and J. B. Goodenough, *Mater. Res. Bull.*, **18**, 461 (1983).
52. Comsol User's Guide version 3.2, Comsol, Inc. (2006).
53. J. A. V. Butler, *Trans. Faraday Soc.*, **19**, 0729 (1924).
54. T. Erdey-Gruz and M. Volmer, *Z. Phys. Chem. Abt. A*, **150**, 203 (1930).
55. J. S. Newman, *Electrochemical Systems*, 2nd ed., p. 560, Prentice–Hall, Englewood Cliffs, NJ (1991).
56. J. Tafel, *Z. Phys. Chem., Stoechiom. Verwandtschaftsl.*, **50**, 641 (1905).
57. A. J. Bard and L. R. Faulkner, *Electrochemical Methods: Fundamentals and Applications*, 2nd ed., p. 95, Wiley, New York (2001).
58. C. M. Doyle, *Design and Simulation of Lithium Rechargeable Batteries*, University of California, Berkeley (1995).
59. X. M. He, J. J. Li, Y. Cai, C. Y. Jiang, and C. R. Wan, *Mater. Chem. Phys.*, **95**, 105 (2006).
60. G. Pistoia and R. Rosati, *J. Power Sources*, **58**, 135 (1996).
61. Z. P. Jiang and K. M. Abraham, *J. Electrochem. Soc.*, **143**, 1591 (1996).
62. G. G. Wang, J. M. Wang, W. Q. Mao, H. B. Shao, J. Q. Zhang, and C. N. Cao, *J. Solid State Electrochem.*, **9**, 524 (2005).
63. B. P. Boudreau, *Geochim. Cosmochim. Acta*, **60**, 3139 (1996).
64. J. F. Brilhac, F. Bensouda, P. Gilot, A. Brillard, and B. Stanmore, *Carbon*, **38**, 1011 (2000).
65. R. A. Macdonald, *Soobshch. Byurak. Obs. Akad. Nauk Arm. SSR*, **68**, 93 (1992).
66. K. J. Duffy, P. T. Cummings, and R. M. Ford, *Biophys. J.*, **68**, 800 (1995).
67. L. Berhan and A. M. Sastry, *J. Compos. Mater.*, **37**, 715 (2003).
68. A. Vallee, S. Besner, and J. Prudhomme, *Electrochim. Acta*, **37**, 1579 (1992).
69. J. E. Weston and B. C. H. Steele, *Solid State Ionics*, **7**, 81 (1982).
70. T. F. Fuller, M. Doyle, and J. Newman, *J. Electrochem. Soc.*, **141**, 982 (1994).
71. http://www.matweb.com/search/SpecificMaterial.asp?bassnum=AMELi00 (2006).
72. http://www.matweb.com/search/SpecificMaterial.asp?bassnumt=NINCO79 (2006).
73. M. C. Lonergan, D. F. Shriver, and M. A. Ratner, *Electrochim. Acta*, **40**, 2041 (1995).
74. N. A. Stolwijk and S. Obeidi, in *Diffusion in Materials: Dimat 2004, Pt 1 and 2*, Vol. 237–240, p. 1004, Trans Tech Ltd., Zurich-Uetikon (2005).
75. L. Q. Chen and J. Schoonman, *Solid State Ionics*, **67**, 17 (1993).
76. W. Weppner and R. A. Huggins, *J. Electrochem. Soc.*, **124**, 1569 (1977).
77. J. Barker, R. Pynenburg, and R. Koksbang, *J. Power Sources*, **52**, 185 (1994).
78. A. H. Thompson, *J. Electrochem. Soc.*, **126**, 608 (1979).
79. Y. Idemoto, T. Mochizuki, K. Ui, and N. Koura, *J. Electrochem. Soc.*, **153**, A418 (2006).
80. D. Zhang, B. N. Popov, and R. E. White, *J. Electrochem. Soc.*, **147**, 831 (2000).
81. K. A. Striebel, C. Z. Deng, S. J. Wen, and E. J. Cairns, *J. Electrochem. Soc.*, **143**, 1821 (1996).
82. F. Y. Shih and K. Z. Fung, *J. Power Sources*, **159**, 179 (2006).
83. P. Arora, M. Doyle, A. S. Gozdz, R. E. White, and J. Newman, *J. Power Sources*, **88**, 219 (2000).
84. C. W. Wang, Y. B. Yi, A. M. Sastry, J. Shim, and K. A. Striebel, *J. Electrochem. Soc.*, **151**, 1489 (2004).
85. http://www.cchem.berkeley.edu/jsngrp/ (2007).
86. Lithium-Ion Battery Charging Cycle Solved with FEMLAB 3.1, COMSOL AB.
87. J. O. Besenhard, *Handbook of Battery Materials*, Wiley-VCH, Weinheim, (1999).
88. B. Scrosati, in *Advances in Li-Ion Batteries*, W. A. van Schalkwijk, B. Scrosati, Editors, p. 251, Kluwer Academic/Plenum, New York (2002).
89. J. Y. Song, Y. Y. Wang, and C. C. Wan, *J. Power Sources*, **77**, 183 (1999).
90. W. L. Zhang, S. Srinivasan, and H. J. Ploehn, *J. Electrochem. Soc.*, **143**, 4039 (1996).
91. N. Cui, J. L. Luo, and K. T. Chuang, *J. Electroanal. Chem.*, **503**, 92 (2001).
92. V. R. Subramanian, H. J. Ploehn, and R. E. White, *J. Electrochem. Soc.*, **147**, 2868 (2000).
93. A. K. Padhi, K. S. Nanjundaswamy, and J. B. Goodenough, *J. Electrochem. Soc.*, **144**, 1188 (1997).
94. V. Srinivasan and J. Newman, *J. Electrochem. Soc.*, **151**, 1517 (2004).
95. P. P. Prosini, *J. Electrochem. Soc.*, **152**, A1925 (2005).
96. L. Laffont, C. Delacourt, P. Gibot, M. Y. Wu, P. Kooyman, C. Masquelier, and J. M. Tarascon, *Chem. Mater.*, **18**, 5520 (2006).
97. J. L. Allen, T. R. Jow, and J. Wolfenstine, *Chem. Mater.*, **19**, 2108 (2007).
98. M. M. Thackeray, Y. Shao-Horn, A. J. Kahaian, K. D. Kepler, J. T. Vaughey, and S. A. Hackney, *Electrochem. Solid-State Lett.*, **1**, 7 (1998).
99. X. Zhang, W. Shyy, and A. M. Sastry, *J. Electrochem. Soc.*, **154**, A910 (2007).